Small-angle p-p elastic scattering at energies between 285 and 572 MeV

D. Aebischer, B. Favier, L. G. Greeniaus, R. Hess, A. Junod,* C. Lechanoine, J. C. Niklès, D. Rapin, C. Richard-Serre,† and D. W. Werren

University of Geneva, Geneva, Switzerland

(Received 18 November 1975)

Differential cross sections for elastic p-p scattering have been measured at 285, 348, 398, 414, 455, 497, 530, and 572 MeV kinetic energy. The experiment was performed at the CERN synchrocyclotron, using multiwire proportional chambers placed directly in a proton beam. Scattering was observed for $1.5° \lesssim \theta \lesssim 10°$ in the laboratory system. The ratio α_p of the real and imaginary parts of the non-spin-flip nuclear forward amplitude was derived from the interference between the Coulomb and nuclear amplitudes. The values obtained are model-dependent, but in this energy range α_p is positive and decreases with energy. Qualitatively good agreement with dispersion-relation predictions is observed.

I. INTRODUCTION

In experiments at very small momentum transfer $0.001 < |t| < 0.05$ (GeV/c)^2, Coulomb scattering as well as its interference with nuclear scattering can be observed. In principle, such measurements allow the magnitude and sign of the ratio α_p of the real and imaginary parts of the forward non-spin-flip nuclear amplitudes to be deduced. At medium energy serious discrepancies have existed between experimental values[1,2] and dispersion-relation calculations[3] of α_p. Recent measurements by Vorobyov *et al.*[4] in the range 500–1000 MeV are in reasonable agreement with these predictions. In this paper, new measurements of the p-p differential cross sections and estimates of α_p, in the energy range from 285 to 572 MeV, are presented. Details can be found in Aebischer's Ph.D. thesis.[5]

The experiment was performed at the CERN synchrocyclotron (SC). Protons were observed before and after scattering from a liquid hydrogen target by means of multiwire proportional chamber (MWPC) telescopes. A fast electronic decision system[6] was used to reject events for which the proton scattering angle was not large enough. The data were obtained under two different sets of experimental conditions. Measurements taken at 398, 455, 497, 530, and 572 MeV kinetic energy are referred to as type I, while measurements taken at 285, 348, and 414 MeV kinetic energy will be named type II.

At the same time that the $d\sigma/d\Omega$ measurements were made, data for the p-p analyzing power $P(\theta)$ in the nuclear-Coulomb interference region were collected,[7] and the inelastic reaction $pp \to \pi^+ d$ was studied at small angles.[8] The apparatus described here has also been used in a slightly modified configuration to measure the carbon analyzing power at several energies.[9]

II GENERAL CONSIDERATIONS

A. Theoretical aspects

For p-p elastic scattering, the S matrix is a 4×4 matrix in spin space. If one takes into account symmetries with respect to time reversal, particle exchange, and parity conservation, the scattering matrix T in the decomposition $S = 1 + 2iT$ can be described by the five helicity amplitudes[10]

$$\begin{aligned}
\varphi_1(4\pi/p^*) &= \langle ++|T|++\rangle = \langle --|T|--\rangle ,\\
\varphi_2(4\pi/p^*) &= \langle ++|T|--\rangle = \langle --|T|++\rangle ,\\
\varphi_3(4\pi/p^*) &= \langle +-|T|+-\rangle = \langle -+|T|-+\rangle ,\\
\varphi_4(4\pi/p^*) &= \langle +-|T|-+\rangle = \langle -+|T|+-\rangle ,\\
\varphi_5(4\pi/p^*) &= \langle ++|T|+-\rangle = \langle +-|T|++\rangle \\
&= \langle --|T|-+\rangle = \langle -+|T|--\rangle \\
&= \langle ++|T|-+\rangle = \langle -+|T|++\rangle \\
&= \langle --|T|+-\rangle = \langle +-|T|--\rangle ,
\end{aligned} \tag{1}$$

where p^* is the c.m. momentum. The ket $|\lambda_a \lambda_b\rangle$ represents a state of two protons in their c.m. system, with helicities λ_a and λ_b. If none of the initial protons are polarized, the differential cross section is written

$$\frac{d\sigma}{d\Omega} = \hbar^2/2\left(\sum_{k=1}^{4} |\varphi_k|^2 + 4|\varphi_5|^2\right) . \tag{2}$$

In the forward direction, both helicity-flip amplitudes $\varphi_4(0)$ and $\varphi_5(0)$ vanish and it is usually more convenient to work with φ_2, and $\varphi_\pm$ defined by

$$\varphi_\pm = \tfrac{1}{2}(\varphi_3 \pm \varphi_1) . \tag{3}$$

Each helicity amplitude is written as a sum of corresponding nuclear (φ_i^N) and Coulomb (φ_i^C) amp-

litudes

$$\varphi_i = \varphi_i^N + \varphi_i^C, \quad i = 2, +, - . \tag{4}$$

The optical theorem then takes the simple form

$$\mathrm{Im}\varphi_+^N = \frac{p^*}{4\pi\hbar^2}\sigma_{\mathrm{tot}} . \tag{5}$$

Using Eqs. (3) and (4), in Eq. (2), the differential cross section in the forward direction can be rewritten[11] as

$$\frac{d\sigma}{d\Omega} = \hbar^2[\,|\varphi_+^N|^2 + |\varphi_-^N|^2 + \tfrac{1}{2}|\varphi_2^N|^2 + 2\,\mathrm{Re}(\varphi_+^{N*}\varphi_+^C + \varphi_-^{N*}\varphi_-^C + \tfrac{1}{2}\varphi_2^{N*}\varphi_2^C)] + \frac{d\sigma^C}{d\Omega} . \tag{6}$$

The last term of Eq. (6) contains only pure Coulomb amplitudes. The φ_i^{N*} are the nuclear scattering amplitudes modified by the electromagnetic force

$$\varphi_i^{N*} = \varphi_i^N \exp(-i\delta_C) . \tag{7}$$

The Coulomb angle δ_C has been calculated nonrelativistically by Bethe[12] as

$$\delta_C = \frac{2}{137\beta}\ln\left(\frac{1.06}{p^* a\theta^*}\right) \simeq 0.03 \text{ rad} , \tag{8}$$

where $a \approx 1$ fermi, and β is the velocity of the proton in the laboratory system. A relativistic expression has been given by Locher[13]

$$\delta_C = \frac{2}{137\beta}\left[\ln\frac{2}{\theta^*} - \ln\left(\frac{2}{3}\right)^{1/2} Rp^* - \frac{\gamma}{2}\right], \tag{9}$$

which yields a similar value of δ_C. Here R is the effective strong-interaction radius and γ is the Euler constant.

For the pure Coulomb interaction, Buttimore[14] has calculated the helicity amplitudes $\varphi_+^C, \varphi_-^C, \varphi_2^C$:

$$\varphi_+^C = \frac{1}{137\sqrt{s}}\,\frac{s-2m^2}{t} ,$$
$$\varphi_-^C = \frac{1}{137\sqrt{s}}\,\frac{2m^2-t}{2u} , \tag{10}$$
$$\varphi_2^C = \frac{1}{137\sqrt{s}}\,\frac{4m^2}{s-4m^2} ,$$

where m is the proton mass. The quantities s, t, and u are the three Mandelstam variables. Only the amplitude φ_+^C is important at small angles, because of its singular behavior in t. Neglecting φ_-^C and φ_2^C, the following contributions to the cross section can be isolated in Eq. (6):

(i) pure Coulomb scattering

$$\left(\frac{d\sigma}{dt}\right)^C = \left(\frac{d\sigma}{d\Omega}\right)^C \frac{\pi}{p^{*2}} = \pi\left(\frac{\hbar}{p^*}\right)^2 |\varphi_+^C|^2 = \left(\frac{2\hbar\sqrt{\pi}}{137\beta t}\right)^2 , \tag{11}$$

(ii) the nuclear non-spin-flip scattering

$$\left(\frac{d\sigma}{dt}\right)_{\mathrm{nf}}^N = \pi\left(\frac{\hbar}{p^*}\right)^2 |\varphi_+^N|^2 , \tag{12}$$

(iii) the nuclear spin-flip scattering

$$\left(\frac{d\sigma}{dt}\right)_{\mathrm{f}}^N = \pi\left(\frac{\hbar}{p^*}\right)^2 (|\varphi_-^N|^2 + 0.5|\varphi_2^N|^2) , \tag{13}$$

(iv) the interference term

$$\left(\frac{d\sigma}{dt}\right)_{\mathrm{int}}^N = 2\pi\left(\frac{\hbar}{p^*}\right)^2 \varphi_+^C(\mathrm{Re}\varphi_+^N + \delta_C \mathrm{Im}\varphi_+^N) . \tag{14}$$

The approximations $\cos\delta_C \simeq 1$ and $\sin\delta_C \simeq \delta_C$ have been used.

B Parametrization

For the fitting procedure, we consider the differential cross section $(d\sigma/d\Omega)(\theta, \vec{\pi})$ to be a function of the scattering angle θ and a set of parameters $\vec{\pi}$ which have to be determined.

In order to find a reasonable parametrization, the nuclear spin-flip and non-spin-flip contributions were calculated from the Livermore phase shifts,[15] and their t dependence in the small-angle region was studied at five incident kinetic energies between 200 and 600 MeV. The following interesting observations can be made

(i) Between 200 and 600 MeV, the imaginary part of the non-spin-flip nuclear amplitude φ_+^N has a nearly perfect exponential t dependence

$$\mathrm{Im}\varphi_+^N(t) = \mathrm{Im}\varphi_+^N(0) e^{Bt/2} . \tag{15}$$

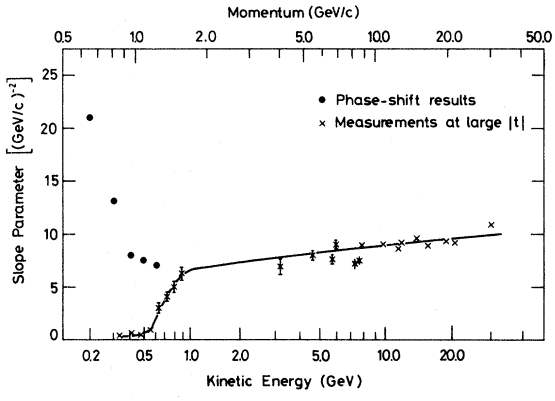

FIG. 1. Comparison of the nuclear slope parameters as a function of energy. The full circles are the slope parameter B of the non-spin-flip nuclear amplitude calculated from the MacGregor phase shifts (Ref. 15). The crosses are slope parameters defined by $d\sigma/dt$ measurements outside the Coulomb-nuclear interference region [from Particle Data Group, Lawrence Radiation Laboratory Report No. UCRL-20 000NN (unpublished). The line is a guide to the eye.

(ii) The ratio of the real and imaginary parts of the non-spin-flip amplitude varies with energy, and is also slightly dependent on t at a given energy in the following manner:

$$\alpha_p(t)=\frac{\mathrm{Re}\varphi_+^N(t)}{\mathrm{Im}\varphi_+^N(t)}=\alpha_0+\alpha' t\,, \tag{16}$$

where α' decreases from 0.03 $(\mathrm{GeV}/c)^{-2}$ at 200 MeV to 0.005 $(\mathrm{GeV}/c)^{-2}$ at 600 MeV.

(iii) The spin-flip nuclear amplitude in our range does not show an exponential behavior with t, but is relatively constant and well described by a second-order polynomial in t.

(iv) The values obtained for the slope parameter B defined by Eq. (15) are shown in Fig. 1. B decreases rapidly with energy from 21 $(\mathrm{GeV}/c)^{-2}$ at 200 MeV, to 8 $(\mathrm{GeV}/c)^{-2}$ at 500 MeV. On the same figure, the values of the conventional slope parameter derived from $d\sigma/dt$ measurements at higher t values, $|t|>0.01$ $(\mathrm{GeV}/c)^2$, are shown. The slope B, calculated from phase shifts, appears to join smoothly with those obtained from $d\sigma/dt$ measurements around 600 MeV. This is probably due to the fact that above 500 MeV, the non-spin-flip amplitude is dominant.

With these observations in mind, we have used two different parametrizations in the analysis of the differential cross sections. They will be referred to as the phase-shift parametrization and the classical parametrization.

The phase-shift parametrization includes the above remarks. Using the optical theorem, the non-spin-flip term becomes

$$\left(\frac{d\sigma}{dt}\right)_{\mathrm{nf}}^N=\frac{\sigma_{\mathrm{tot}}^2}{16\pi\hbar^2}[1+(\alpha_0+\alpha' t)^2]e^{Bt}\,, \tag{17}$$

while the interference term is written as

$$\left(\frac{d\sigma}{dt}\right)_{\mathrm{int}}=\frac{\sigma_{\mathrm{tot}}}{137\beta t}(\alpha_0+\alpha' t+\delta_C)e^{Bt/2}\,. \tag{18}$$

The spin-flip contribution is

$$\left(\frac{d\sigma}{dt}\right)_{\mathrm{f}}^N=a_0+a_1 t+a_2 t^2\,, \tag{19}$$

where a_0, a_1, a_2 are coefficients. The set of parameters $\vec{\pi}$ considered is $(B,\alpha_0,\alpha',a_0,a_1,a_2)$. Table I summarizes the values found for these parameters in the phase-shift calculations.

The classical parametrization has usually been used in other similar experiments.[1,2,4] In this method, the spin-flip and non-spin-flip nuclear cross sections are presumed to be proportional and to have the same exponential t dependence, i.e.,

$$\left(\frac{d\sigma}{dt}\right)_{\mathrm{f}}^N=\rho^2\left(\frac{d\sigma}{dt}\right)_{\mathrm{nf}}^N(0)e^{bt} \tag{20}$$

The value for the slope parameter is derived from experiments at $|t|>0.01$ $(\mathrm{GeV}/c)^2$, which give a small value $b\lesssim 2$ $(\mathrm{GeV}/c)^{-2}$ in our energy range. The t dependence of α_p is usually neglected. The parameter set $\vec{\pi}$ then consists of (b,ρ^2,α_p).

III. EXPERIMENTAL METHOD

Most of the data were taken under type I conditions, so mainly this experimental setup will be described here. More details about the type I experimental equipment can be found in Ref. 9. A complete description of the type II experiment can be found in Ref. 5. Table II summarizes the differences in the beams and detection apparatus in the two series of measurements.

A. Beam transport system

To obtain the 572-, 455-, and 398-MeV beams, a 595-MeV unpolarized proton beam with an intensity of $\simeq 10^{11}$ protons/sec was extracted from the CERN SC and polarized by scattering at 7° on a carbon target. The transverse polarization vector could be reversed by changing the sense of the scattering. To lower the beam energy to 455 and

TABLE I. Values of the parameters for the phase-shift parametrization as determined from an existing phase-shift analysis (See Ref. 15).

Energy (MeV)	B $[(\mathrm{GeV}/c)^{-2}]$	α_0	α' $[(\mathrm{GeV}/c)^{-2}]$	a_0 $[\mathrm{mb}(\mathrm{GeV}/c)^{-2}]$	a_1 $[10^3\ \mathrm{mb}(\mathrm{GeV}/c)^{-4}]$	a_2 $[10^6\ \mathrm{mb}(\mathrm{GeV}/c)^{-6}]$	σ_{tot} (mb)
285	14.0	0.75	23.5	78	2.75	1.80	24.0
348	10.0	0.55	19.0	64	2.13	1.10	24.6
398	8.2	0.41	16.0	52	1.65	0.75	25.6
414	7.8	0.37	15.5	48	1.50	0.67	27.0
455	7.6	0.27	13.0	40	1.20	0.49	28.5
497	7.4	0.17	10.5	31	0.92	0.38	30.5
530	7.3	0.10	9.0	26	0.76	0.34	32.6
572	7.2	0.02	6.5	22	0.60	0.30	36.0

TABLE II. Differences between type I and type II experiment.

	Type I experiment	Type II experiment
Beams:		
Mean interaction energies	398, 455, 497, 530, 572 MeV	285, 348, and 414 MeV
Polarization	At 398, 455, and 572 MeV, $P_0 = 0.376 \pm 0.015$. At 497 MeV, $P_0 = 0.433 \pm 0.023$. At 530 MeV, $P_0 = 0.313 \pm 0.033$.	At 285 MeV and 348 MeV $P_0 = 0$. At 414 MeV $P_0 \simeq 0.40$.
Intensity	10^4–10^5 protons/sec.	$<10^4$ protons/sec.
Telescopes:		
Forward telescope	2 MWPC before LH_2 (M1–M2)	Same as for type I
Backward telescope	4 MWPC after LH_2 (M3–M6) with M6 rotated by 45° Both telescopes fixed.	3 MWPC after LH_2 (M3–M5) with M4 rotated by 45° Backward telescope could be turned by about 2° around the Y axis.
Acceptance >95%	$\theta_{lab} \lesssim 6.5°$	$\theta_{lab} \lesssim 2.0°$ if turned $\theta_{lab} \lesssim 3.5°$ if straight
Counters: A, B, E, T, X	A, B trigger counters E: $100 \times 100 \times 5$ mm^3 T: $500 \times 500 \times 10$ mm^3 X: $500 \times 500 \times 20$ mm^3	Same as for type I E did not exist T did not exist X: $300 \times 300 \times 10$ mm^3
Acquisition		
On-line computer	IBM 1800 or PDP 11/20	IBM 1800
Electronics	Fast decision rejected unscattered events in 1–2 μsec.	No fast decision. Scattering angle calculated by the computer on-line.
Recorded event rates	100–200 events/sec	1–10 events/sec

398 MeV, degraders of B_4C were used before the last bending magnet. Momentum resolution was about ±1%. The 530- and 497-MeV beams were comprised of protons scattered from an internal target into the SC extraction channel. At all these energies, a solenoid permitted the azimuthal orientation of the polarization vector to be modified by an angle $\phi_0 = \pm(35° - 45°)$.

Two methods were used to calibrate the beam energies. Differential range curve measurements were made at 572, 455, 414, 348, and 285 MeV. For the type I measurements only, a second independent method was provided by the inelastic $pp \to \pi^+ d$ events where both the π and d tracks were detected. A fit to the correlation between the π and d scattering angles, $\theta_\pi = f(\theta_d)$, allowed each beam energy to be determined with errors of ±2 MeV. The two methods are in excellent agreement. The quoted mean interaction energies are those obtained by the kinematic fit to the $pp \to \pi^+ d$ events since this method gave the most precise results.

B. Detection apparatus

A scale drawing of the apparatus is shown in Fig. 2. The system is axially symmetric with a 90° period for rotations about the beam axis. Two multiwire proportional chamber telescopes (M1–M2 and M3–M6) were placed directly in the beam on either side of a LH_2 target to allow the incoming and scattered proton trajectories to be reconstructed. All the MWPC provided horizontal (X) and vertical (Y) coordinates in the laboratory, except M6 which was rotated by 45° about the beam axis. Chamber M6 was used in the study of the inelastic reaction $pp \to \pi^+ d$ in order to resolve ambiguities due to multiple tracks in the backward

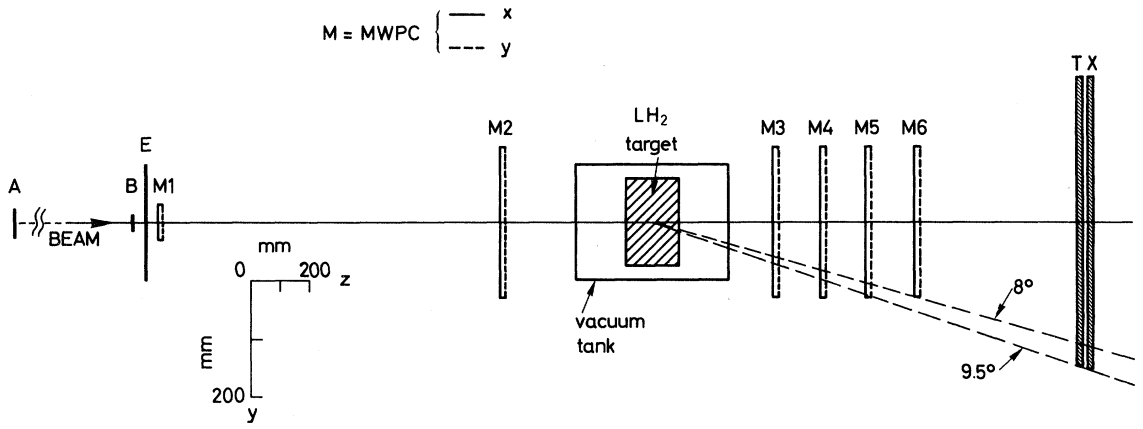

FIG. 2. Scale drawing of the apparatus (side view). M1–M6 are multiwire proportional chambers. A, B, E, T, and X are scintillation counters. The beam comes from the left. Notice the different horizontal and vertical scales.

telescope. The horizontal and vertical positions of all six MWPC were calibrated during special runs by observing undeflected tracks and requiring that the hit coordinates be properly aligned. Typical plane efficiencies were over 98%.

The liquid hydrogen target was 15 cm in diameter and 16.7 cm long. This length was chosen so that the multiple scattering in the LH_2 would be comparable to the spatial resolution of the telescopes. The over-all angular resolution of the system was about 0.25° at 572 MeV. Only ~1% of the incident protons interacted in the target.

Five scintillation counters A, B, E, T, and X were used. The time of flight of the scattered particles was measured between counters B and X. Counters X and T, which were each observed by one horizontal phototube, provided dE/dX measurements of the scattered particles. The coincidence $ABXT$ was used to trigger the system, while a second coincidence EX within the resolving time of the MWPC system was used to veto events with a second beam particle.

C. Electronics and data acquisition

A fast hardware logic designed for this experiment allowed events to be rejected when the proton was deflected by less than 1.5° in the LH_2 target, thereby eliminating 99% of the undesired events. This fast (1 – 2 μsec) decision system has been described in detail in previous articles.[6,9,16] An extensive CAMAC system allowed the experiment to be monitored by an on-line computer, which also recorded the accepted events on magnetic tape.

Approximately equal numbers of events were obtained for each orientation of beam polarization at a given energy. With a beam of 10^4 protons/sec, about 100–200 events/sec were recorded. Background from scattering in the air and mylar target windows was estimated from runs with a dummy empty target. The dummy target had slight structural differences from the real target, which were compensated for in the analysis which is discussed later.

IV. DATA ANALYSIS

A. Selection criteria

All raw events accepted by the fast decision system were reconstructed in an off-line analysis. Track reconstruction of the scattered tracks required at least five planes out of the eight possible. Events used to calculate the differential cross sections satisfied the following criteria:

(i) Exactly one track could be reconstructed from the hit coordinates in both telescopes. Good incident tracks were selected by hardware. In the off-line analysis, 5–10 % of the raw events were eliminated, corresponding to cases where it was impossible to align five sparks, or where two tracks were reconstructed in the rear telescope.

(ii) The number of planes with multiple hits in the backward telescope had to be <3. This eliminated possible two-track events for which the second track was emitted at a relatively large angle and not seen by a sufficient number of planes to be reconstructed. For part of the data, this cut was made by the fast decision system. For the remainder it was a software cut.

(iii) A χ^2-like figure of merit was defined for the reconstructed track. A limit given by

$$Q^2 = \frac{1}{n-4} \sum_n (W_f - W_m)^2 < 1.7 \text{ mm}^2 \qquad (21)$$

was required. The W's are fitted and measured coordinates and n is the number of planes used in the fit. About 1–2% of the one-track events were rejected, mainly due to scattering in the rear wire chambers.

(iv) The beam size at the middle of the LH_2 target was limited to

$$(X^2+Y^2)<(35\ \text{mm})^2 \tag{22}$$

in order to facilitate acceptance calculations. This eliminated about 4% of the one-track events.

(v) The interaction point along the beam axis, defined by the incident and scattered tracks, had to lie in the range $-207<Z_v<200$ mm. Figure 3 shows typical Z_v distributions for LH_2 target data and dummy target data normalized to the same number of incident particles. For one-track events, 55% of the LH_2 data and 80% of the dummy data were rejected, mainly because the proton scattered in chamber M2.

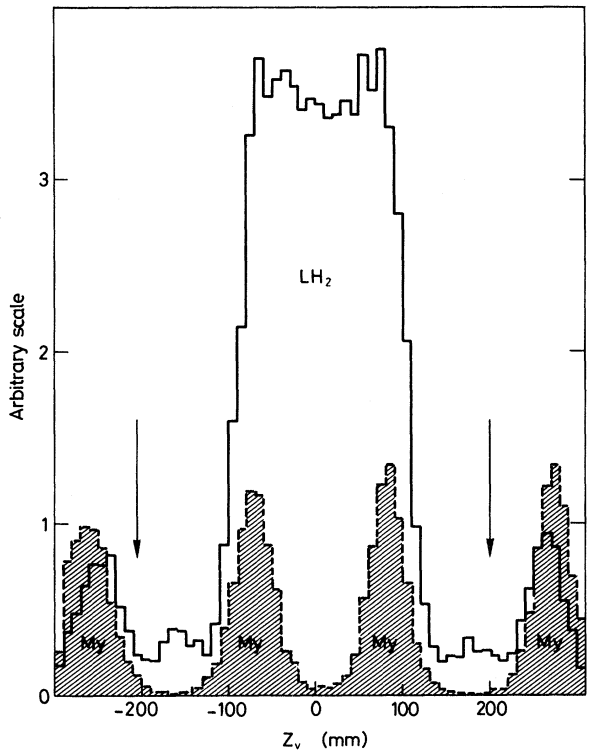

FIG. 3. Distribution of the interaction vertex (Z_v) along the beam axis at 455 MeV for $2.5°<\theta<6.5°$. The shaded areas correspond to dummy target data normalized to the same number of incident tracks as for the LH_2 data. The differences in the distribution of events from the Mylar (My) windows are due to technical differences between the two targets and the different multiple scattering. The arrows indicate the cuts applied to the data ($-207<Z_v<200$ mm).

(vi) The minimum distance between the incoming and the outgoing tracks had to be <6 mm. About 3% of the one-track events were rejected, mainly eliminating events which had scattered in one of the MWPC telescopes.

(vii) All tracks had to lie inside the sensitive region of wire chambers M3–M5. Events that passed through the frames of the rotated chamber (M6) were rejected.

(viii) Measurements of time of flight (TOF) and energy loss (dE/dX) in the counters X and T were used to eliminate events due to inelastic reactions. The measured values of time of flight and dE/dX were corrected for time drifts and spatial dependence on the impact point in the counters. The impact point was defined by the projection of the reconstructed track into the counter plane. These corrections were typically $\lesssim 5\%$ and always less than 20%. Figure 4 shows a typical corrected TOF dE/dX plot. The data were cut in the region between the proton and deuteron peaks. Excellent rejection of the two-body inelastic events $pp\to\pi^+d$ was achieved. In our energy range. the deuteron always appears in a forward cone ($\theta_{\text{lab}}<12°$) and at a given θ_{lab}, there are deuterons emitted backwards and forwards in the c.m. system. Not all three-body inelastic events ($pp\to pn\pi^+$ and $pp\to pp\pi^0$) could be discriminated against. Particles from the three-body inelastic reactions have continuous velocity spectra which extend into the region of the elastically scattered protons, and not all these events are eliminated by the cut. This remaining inelastic contamination was taken into account in deriving the final p-p elastic cross sections.

B. Acceptance correction

For most of the polar angles where data have been obtained, the full 2π azimuthal range was observed. However, for the larger angles, the geometrical acceptance was less than 100% and the measured cross sections $(d\sigma/d\Omega)_m$ had to be corrected for the loss of solid angle. These corrections were determined by Monte Carlo techniques.

Simulated p-p elastic events were generated and tracked through the system. In order to take properly into account the beam divergence and the beam displacement produced by changing the field in the solenoid, incident tracks were taken at random from the experimental data where the lab scattering angle was less than 5°. For the simulated scattering in the LH_2 target, a uniform azimuthal distribution was generated, but in order to improve the statistical errors of the corrections, the number of events as a function of θ was peaked in the region where the geometrical acceptance decreases. Therefore, the experimental scatter-

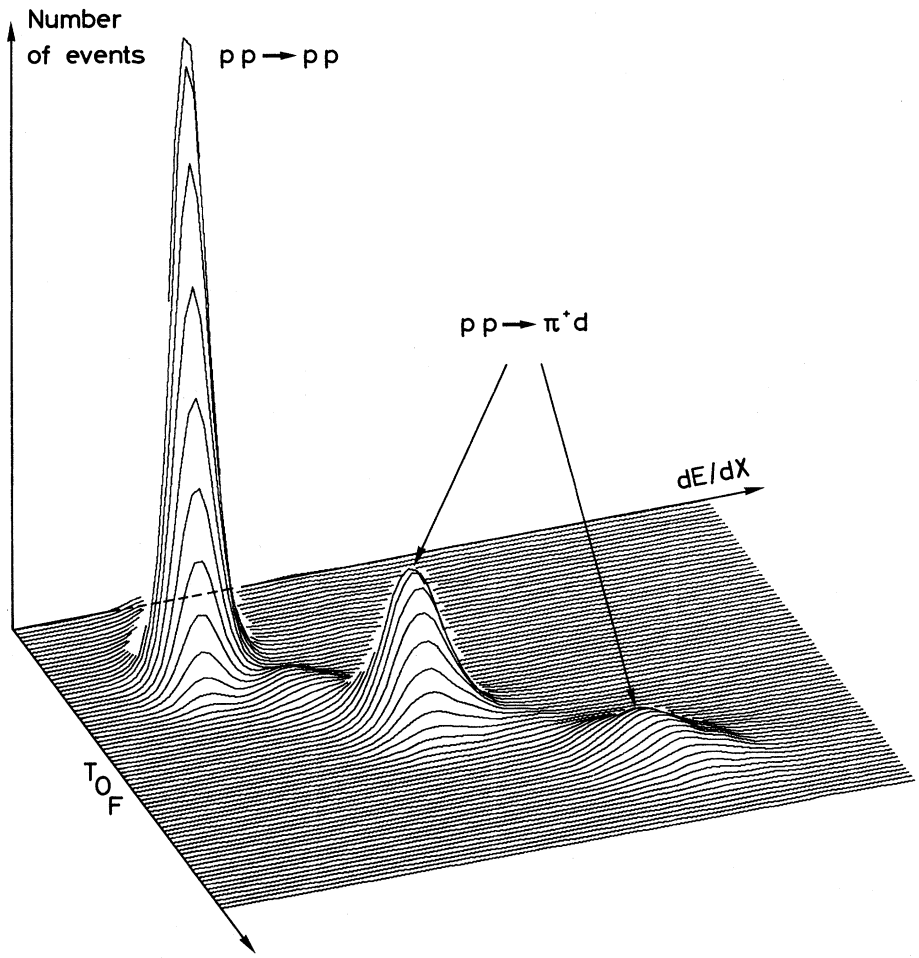

FIG. 4. Correlation between the corrected time of flight (TOF) and energy loss (dE/dX) measurements in the counters X and T at 455 MeV. The elastic proton peak and the two deuteron peaks from the inelastic reaction $pp \rightarrow \pi^+ d$ can be seen. The contribution from the three-body inelastic reactions forms the continuous background passing under the three main peaks.

ing distributions were not duplicated, but this does not affect calculations of the desired corrections. Multiple scattering was included and hits in all MWPC were generated. The event was reconstructed as for the real data and the same geometrical cuts were applied. A purely geometrical acceptance correction defined by $\bar{A}(\theta) = N_a(\theta)/N_g(\theta)$ was calculated. $N_a(\theta)$ and $N_g(\theta)$ are the number of accepted and generated Monte Carlo events, respectively.

With a polarized beam, $(d\sigma/d\Omega)_m$ is a function of the range of azimuthal angle observed. The fraction of detected events, given by an acceptance function $A(\theta, \phi)$, depends both on the scattering angle θ and the azimuthal angle ϕ. The measured cross section can be written

$$\left(\frac{d\sigma}{d\Omega}\right)_m(\theta) = \frac{1}{2\pi}\int_0^{2\pi} \frac{d\sigma}{d\Omega}(\theta)[1 + P_0 P(\theta)\cos(\phi + \phi_0)]A(\theta, \phi)d\phi\,, \tag{23}$$

where $P(\theta)$ is the analyzing power of hydrogen and ϕ_0 is the angle between $\vec{P}_0$ and the vertical axis of the system. This can be rewritten as

$$\left(\frac{d\sigma}{d\Omega}\right)_m(\theta) = \frac{d\sigma}{d\Omega}(\theta)\bar{A}(\theta)\left(1 + P_0 P(\theta)\int_0^{2\pi} \cos(\phi + \phi_0)\frac{A(\theta, \phi)}{\bar{A}(\theta)}d\phi\right), \tag{24}$$

with

$$\bar{A}(\theta)=\frac{1}{2\pi}\int_0^{2\pi} A(\theta,\phi)d\phi\,. \tag{25}$$

The integral in Eq. (24) is estimated from the simulated events.

$$I(\theta)=\int_0^{2\pi}\cos(\phi+\phi_0)\frac{A(\theta,\phi)}{\bar{A}(\phi)}d\phi$$
$$=\frac{\sum_a\cos(\phi+\phi_0)}{N_a(\theta)}, \tag{26}$$

where $\sum_a$ means that the sum is made over the accepted events. $\cos(\phi+\phi_0)$ is the appropriate weight to use for Monte Carlo events with a uniform ϕ distribution. When the acceptance is 100%, the expectation of $I(\theta)$ is zero. The effect of the polarized beam can be interpreted as a modification to the purely geometrical acceptance which becomes

$$\bar{A}'(\theta)=\bar{A}(\theta)[1+P_0P(\theta)I(\theta)]\,. \tag{27}$$

The error $\delta\bar{A}'$ is given by

$$\delta^2\bar{A}'=\delta^2\bar{A}[1+P_0P(\theta)I(\theta)]^2$$
$$+[\bar{A}(\theta)P_0P(\theta)]^2\delta^2I\,, \tag{28}$$

with

$$\delta^2I=[\langle\cos^2(\phi+\phi_0)\rangle-\langle\cos(\phi+\phi_0)\rangle^2]/N_a(\theta)\,. \tag{29}$$

Separate Monte Carlo calculations have been made for the hydrogen data acceptance $\bar{A}_H(\theta)$ and for the dummy acceptance $\bar{A}_D(\theta)$ in order to take into account the differences between the two targets. Figure 5 shows the geometrical acceptance for the H_2 and dummy data at 398 MeV (type I experiment), and at 414 MeV (type II experiment). The acceptance depends mainly on the beam properties, and not on the energy. Acceptances at different energies in the type I setup do not differ by more than 0.03.

For data taken with orientations of beam polarization differing by 180°, $I(\theta)$ changes sign but is equal in absolute value. Thus the effects of beam polarization can be eliminated by combining data with equal statistics and opposite spin directions.

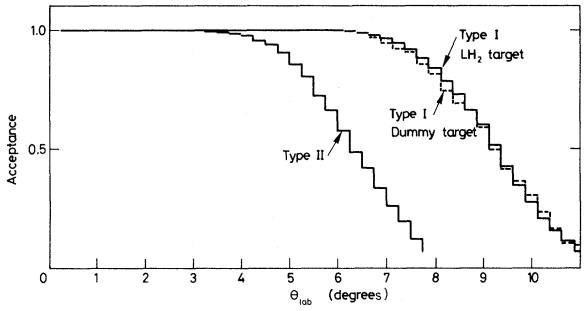

FIG. 5. Geometrical acceptance of the system as a function of the lab scattering angle. The type I curves are calculated at 398 MeV. The type II curve refers to the hydrogen data at 414 MeV. Variations at different energies are less than 0.03 and are due mainly to changes in the shape of the incident beam.

This was possible for the data taken at 398, 455, and 572 MeV. At 497 and 530 MeV, beam polarizations of opposite directions were not available and the measured differential cross sections have been corrected for the effects of the beam polarization. For a lab scattering angle of 9° at 530 MeV, after summing over all available spins, $I(\theta)=+0.07$, resulting in a change of +0.009 to the geometrical acceptance.

C. Measured differential cross sections

The measured lab p-p differential cross sections corrected for geometrical acceptance and for background due to interactions on materials other than the liquid hydrogen are given by

$$\left(\frac{d\sigma}{d\Omega}\right)_m(\theta)=K\left(\frac{N_H(\theta)}{\bar{A}_H(\theta)}-\frac{QN_D(\theta)}{\bar{A}_D(\theta)}\right)(2\pi\sin\theta\,\Delta\theta)^{-1}\,. \tag{30}$$

K is a normalization constant to be determined later in the fitting procedure. $N_H(\theta), N_D(\theta)$ are the total number of events observed in the angle range $\theta\pm\Delta\theta/2$ for target full and dummy data, respectively. Q is a factor to normalize $N_D(\theta)$ and $N_H(\theta)$ to the same number of incident particles. The error δ_m in $(d\sigma/d\Omega)_m$ is given by

$$\delta_m^2(\theta)=\left(\frac{K}{2\pi\sin\theta\,\Delta\theta}\right)^2\left[\frac{N_H(\theta)}{\bar{A}_H^2(\theta)}\left(1+\frac{\delta^2\bar{A}_HN_H(\theta)}{\bar{A}_H^2(\theta)}\right)+\frac{Q^2N_D(\theta)}{\bar{A}_D^2(\theta)}\left(1+\frac{\delta^2\bar{A}_DN_D(\theta)}{\bar{A}_D^2(\theta)}\right)\right]\,. \tag{31}$$

V. CORRECTIONS TO THE DATA

In order to find the true differential cross sections $d\sigma/d\Omega$, the following effects had to be considered: (i) contamination from the three-body inelastic reactions, (ii) multiple and plural scattering in the LH_2 target, (iii) angular resolution of the two MWPC telescopes, and (iv) binning effects in the histogram procedure used. A detailed study of these effects is necessary because they smooth out the angular distribution and mask the structure of the interference between the very steep Coulomb and the almost flat nuclear scattering. Corrections (ii) and (iii) imply deconvolu-

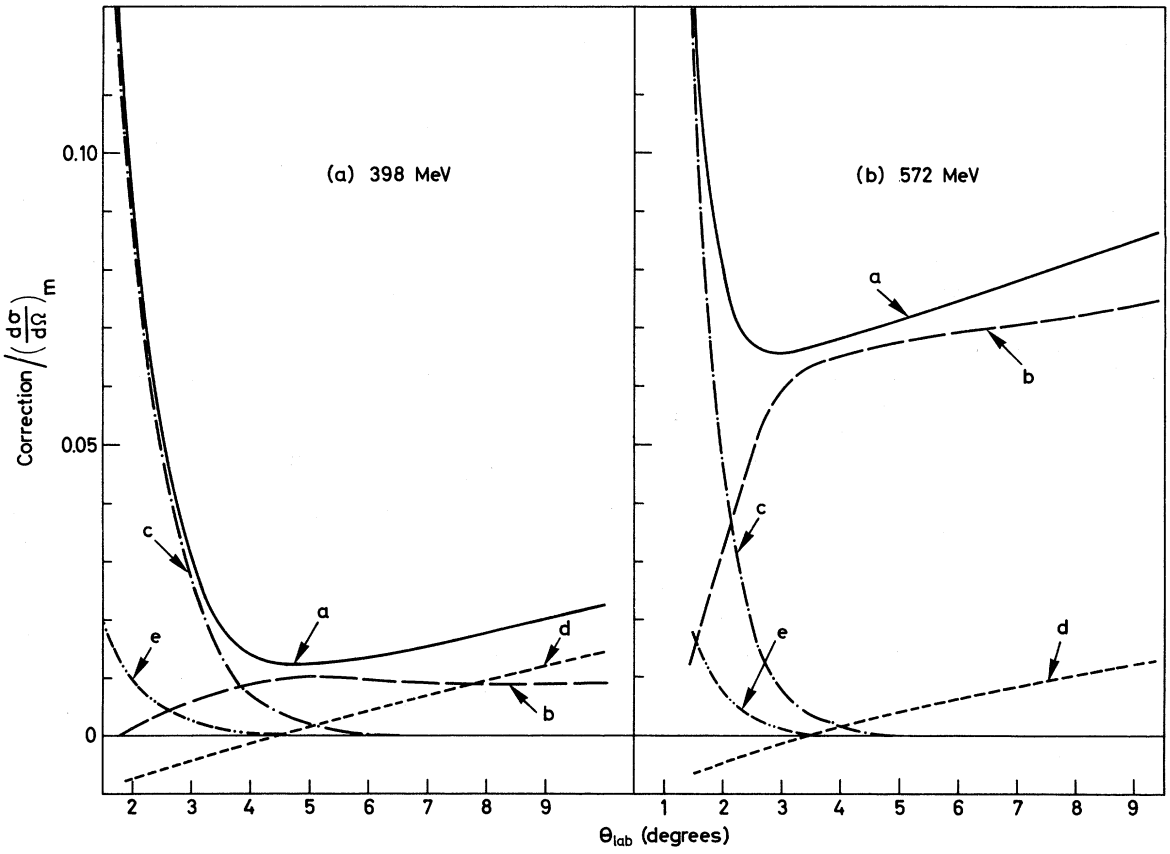

FIG. 6. Relative importance of the corrections to the measured differential cross sections at (a) 398 MeV and (b) 572 MeV. The corrections are obtained from fits using the phase-shift parametrization. Curve b presents the estimated remaining three-body inelastic contamination. Curves c and d are the corrections that are respectively independent and dependent on the parameters $\vec{\pi}$. Curve e is the correction due to the variation of $d\sigma/d\Omega$ inside the 0.25° wide angular bins. Curve a is the algebraic sum of all the fractional corrections.

tion of the experimental distributions. This is a delicate problem since the raw data only extend over a finite angular range and have inherent statistical fluctuations.

The differential cross sections measured are described by Eq. (11)–(14). The set of parameters $\vec{\pi}$ defined by Eq. (15)–(19) have been determined by comparison of the experimental results to the parametrized cross sections $(d\sigma/d\Omega)(\theta, \vec{\pi})$. Instead of attacking the difficult problem of deconvolution, a Molière function $M_H(\theta)$ for the multiple scattering in the LH_2 and a function $R(\theta)$ describing the telescope resolutions have been convoluted with $(d\sigma/d\Omega)(\theta, \vec{\pi})$ before comparison with the measured cross sections. An iterative procedure was necessary since the results of the convolution depend on the parameters $\vec{\pi}$.

The parametrized cross sections were first corrected for contamination from three-body inelastic events in the data and then the convolution was made. A function similar to

$$F(\theta_i, \vec{\pi}) = R * M_H * \left(\frac{d\sigma}{d\Omega}(\vec{\pi}) + C_{inel}\right) \tag{32}$$

was used to approximate the measured cross sections. The asterisk indicates a convolution which depends only on the angular variables. The functions used have cylindrical symmetry. In this case the convolution is defined by

$$f * g(\theta_i) = \frac{1}{2\pi} \int_0^{2\pi} \int_0^{\pi} g(\theta) f((\theta^2 + \theta_i^2 - 2\theta\theta_i \cos\phi)^{1/2})\, d\Omega\,. \tag{33}$$

A more rigorous form of Eq. (32) was actually used to approximate the measured cross sections

$$F(\theta_i, \vec{\pi}) = R * \left\{ M_H * \left[\frac{d\sigma}{d\Omega} - \left(\frac{d\sigma}{d\Omega} \right)^C + C_{\text{inel}} \right] + M_H / N_{at} \right\} + C_B \,. \tag{32'}$$

Here N_{at} is the number of atoms per unit area in the target. This equation is more rigorous because the Molière distribution contains the effects of all Coulomb scattering. The correction due to binning of the data (C_B) is the difference between the average value of the function in a bin and the value at the center of the bin. It is treated as an additive constant for each bin. The over-all correction coefficient $C(\theta_i, \vec{\pi})$ is defined from Eq. (32′) by

$$F(\theta_i, \vec{\pi}) = \left(\frac{d\sigma}{d\Omega} + C_{\text{inel}} \right) + C(\theta_i, \vec{\pi}) \,. \tag{34}$$

Values of the parameters $\vec{\pi}$ are obtained by minimizing the quantity

$$\chi^2 = \sum_i \left[F(\theta_i, \vec{\pi}) - \left(\frac{d\sigma}{d\Omega} \right)_m (\theta_i) \right]^2 \Big/ \delta_m^2(\theta_i) \,. \tag{35}$$

The individual corrections are treated in detail below.

A. Corrections due to the three-body inelastic reactions (C_{inel})

Contamination from these reactions has been evaluated by Monte Carlo simulation because very little experimental information exists. It has been assumed that the three-body events pass through the intermediate state ΔN (i.e., $pp \to \Delta N \to NN\pi$), where the $\Delta(1236)$ resonance is distributed isotropically in the center of mass. The estimated differential cross sections of contaminating events (C_{inel}) were determined by normalizing the simulated distributions using the total cross sections given in a Saclay compilation.[17] For contaminating events, the velocity of the small-angle particle had to be similar to that of elastically scattered protons. For energies >400 MeV, our final sample is mainly contaminated by the π^+ or the p from the reaction $pp \to pn\pi^+$; the two protons from the reaction $pp \to pp\pi^0$ account for only $\frac{1}{6}$ of the background. The maximum percent contamination increased with energy from 1% at 398 MeV up to 7% at 572 MeV. This correction is independent of the parameters $\vec{\pi}$. The angular dependence of the contamination relative to $(d\sigma/d\Omega)_m$ at 398 and 572 MeV is shown in Fig. 6.

B. Corrections due to multiple scattering in the hydrogen target (C_M)

The usual Gaussian approximation for multiple scattering is inadequate here since it is necessary to take into account the effect of plural scattering. A Molière function[18] given by

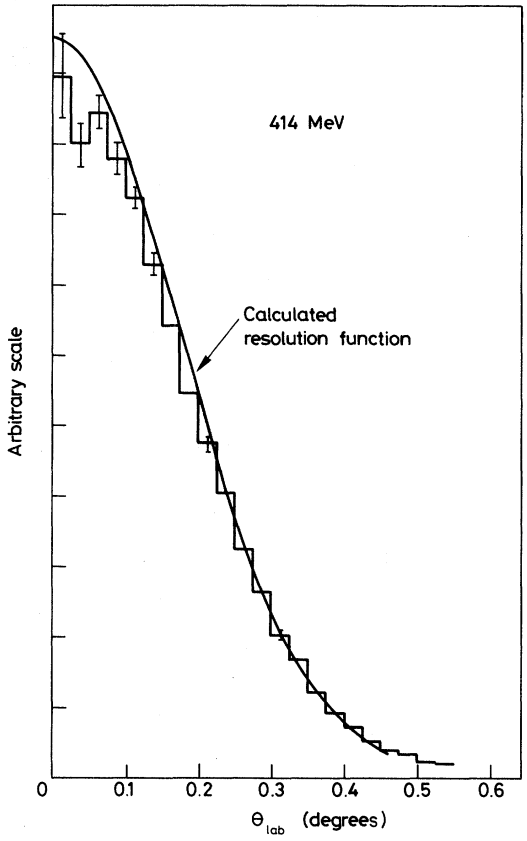

FIG. 7. Comparison between the observed angular distribution of the protons passing through the system and the calculated resolution function at 414 MeV. The experimental distribution is obtained by dividing the number of observed events in each angular bin by the corresponding solid angle.

TABLE III. Summary of differential cross sections. Beam energy = 285 ± 4 MeV, beam spread = ± 10 MeV half width at half maximum (HWHM). The correction due to binning (C_B) is the difference between the total correction and the sum of all other corrections given below.

θ_{lab} (degrees)	Measured $\left(\frac{d\sigma}{d\Omega}\right)_m \pm \delta_m$ (mb/sr)	C_{inel} (mb/sr)	Corrections to $(d\sigma/d\Omega)_m$ $\frac{H(\theta)}{(d\sigma/d\Omega)_m}$ (%)	$\frac{G(\theta)}{(d\sigma/d\Omega)_m}$ (%)	$\frac{C}{(d\sigma/d\Omega)_m}$ (%)	Corrected $\frac{d\sigma}{d\Omega}$ (mb/sr)
2.125	155.63 ± 2.53	0	−1.2	12.8	12.7	135.90
2.375	96.70 ± 1.90	0	−1.2	10.4	10.0	87.07
2.625	61.66 ± 1.47	0	−1.2	8.9	8.2	56.62
2.875	44.49 ± 1.20	0	−1.2	7.0	6.3	41.70
3.125	34.83 ± 1.02	0	−1.1	5.4	4.6	33.21
3.375	25.88 ± 0.87	0	−1.1	4.6	3.7	24.91
3.625	22.72 ± 0.79	0	−0.9	3.4	2.7	22.12
3.875	19.96 ± 0.73	0	−0.8	2.6	1.9	19.58
4.125	17.99 ± 0.68	0	−0.6	2.0	1.4	17.74
4.375	18.83 ± 0.67	0	−0.4	1.3	1.0	18.65
4.625	17.79 ± 0.67	0	−0.3	1.0	0.7	17.66
4.875	17.19 ± 0.62	0	−0.2	0.8	0.6	17.09
5.125	14.87 ± 0.61	0	−0.1	0.7	0.6	14.78
5.375	15.40 ± 0.60	0	0	0.5	0.5	15.32
5.625	16.05 ± 0.62	0	0.1	0.4	0.5	15.98
5.875	15.67 ± 0.64	0	0.2	0.3	0.5	15.59
6.125	15.56 ± 0.69	0	0.3	0.2	0.5	16.48
6.375	16.77 ± 0.73	0	0.4	0.2	0.6	16.68
6.625	15.46 ± 0.73	0	0.5	0.1	0.6	15.37
6.875	15.38 ± 0.75	0	0.5	0.1	0.6	15.28
7.125	16.63 ± 0.83	0	0.6	0.1	0.7	16.52
7.375	15.56 ± 0.89	0	0.7	0.1	0.8	15.45

TABLE IV. Summary of differential cross sections. Beam energy = 348 ± 4 MeV, beam spread = ± 5 MeV (HWHM). The correction due to binning (C_B) is the difference between the total correction and the sum of all other corrections given below.

θ_{lab} (degrees)	Measured $\left(\frac{d\sigma}{d\Omega}\right)_m \pm \delta_m$ (mb/sr)	C_{inel} (mb/sr)	Corrections to $(d\sigma/d\Omega)_m$ $\frac{H(\theta)}{(d\sigma/d\Omega)_m}$ (%)	$\frac{G(\theta)}{(d\sigma/d\Omega)_m}$ (%)	$\frac{C}{(d\sigma/d\Omega)_m}$ (%)	Corrected $\frac{d\sigma}{d\Omega}$ (mb/sr)
2.125	112.39 ± 2.02	0.33	−0.9	8.8	9.1	102.17
2.375	71.47 ± 1.56	0.33	−0.9	7.0	7.3	66.28
2.625	50.03 ± 1.23	0.33	−0.8	5.4	5.8	47.14
2.875	38.72 ± 1.05	0.33	−0.7	4.0	4.5	36.97
3.125	30.19 ± 0.91	0.32	−0.7	3.1	3.9	29.03
3.375	27.02 ± 0.80	0.32	−0.5	2.2	3.1	26.19
3.625	23.10 ± 0.76	0.32	−0.4	1.7	2.7	22.47
3.875	20.69 ± 0.72	0.32	−0.3	1.3	2.5	20.17
4.125	21.24 ± 0.69	0.32	−0.2	0.8	2.1	20.79
4.375	19.20 ± 0.67	0.31	−0.1	0.6	2.2	18.77
4.625	20.05 ± 0.65	0.31	0	0.5	2.1	19.63
4.875	20.30 ± 0.65	0.31	0.1	0.3	2.0	19.90
5.125	19.05 ± 0.65	0.31	0.2	0.3	2.0	18.67
5.375	19.33 ± 0.64	0.31	0.2	0.2	1.9	18.96
5.625	18.14 ± 0.65	0.30	0.3	0.2	2.1	17.76
5.875	18.86 ± 0.67	0.30	0.4	0.1	2.1	18.46
6.125	17.05 ± 0.69	0.30	0.5	0.1	2.3	16.65
6.375	18.12 ± 0.70	0.30	0.6	0.1	2.2	17.72
6.625	18.46 ± 0.72	0.30	0.6	0.1	2.2	18.06
6.875	19.44 ± 0.78	0.29	0.5	0.0	2.2	19.02
7.125	18.36 ± 0.75	0.29	0.7	0.0	2.3	17.94
7.375	19.33 ± 0.90	0.29	0.7	0.0	2.2	18.91

$$M_H(\theta) = [2e^{-(\theta/\theta_H)^2} + f_1(\theta/\theta_H)/B_H + f_2(\theta/\theta_H)/B_H^2]/\theta_H^2 \quad (36)$$

was used. The parameters θ_H and B_H, calculated with the Fano correction, depend on the thickness of the LH_2 target. The correction $C_M(\theta)$ to the parametrized differential cross section due to multiple scattering is given by

$$C_M(\theta) = \left[\frac{M_H}{N_{at}} - \left(\frac{d\sigma}{d\Omega}\right)^C\right] + M_H * \left[\frac{d\sigma}{d\Omega} - \left(\frac{d\sigma}{d\Omega}\right)^C + C_{inel}\right] - \left[\frac{d\sigma}{d\Omega} - \left(\frac{d\sigma}{d\Omega}\right)^C + C_{inel}\right] . \quad (37)$$

At small angles, $d\sigma/d\Omega$ is essentially a Rutherford distribution. Thus the corrections should be largest at small angles. However, since the smallest angle measured in the experiment is large with respect to $\theta_H(\simeq 0.2°)$, the corrections never exceed 15%.

C. Corrections due to the angular resolution of the MWPC telescopes (C_R)

The correction due to the angular resolution of the telescopes is a convolution given by

TABLE V. Summary of differential cross sections. Beam energy = 398 ± 2 MeV, beam spread = ± 5 MeV (HWHM). The correction due to binning (C_B) is the difference between the total correction and the sum of all other corrections given below.

θ_{lab} (degrees)	Measured $\left(\frac{d\sigma}{d\Omega}\right)_m \pm \delta_m$ (mb/sr)	C_{inel} (mb/sr)	Corrections to $(d\sigma/d\Omega)_m$ $\frac{H(\theta)}{(d\sigma/d\Omega)_m}$ (%)	$\frac{G(\theta)}{(d\sigma/d\Omega)_m}$ (%)	$\frac{C}{(d\sigma/d\Omega)_m}$ (%)	Corrected $\frac{d\sigma}{d\Omega}$ (mb/sr)
1.75	212.80 ± 1.89	0.20	−0.8	12.1	12.8	185.63
2.00	121.62 ± 1.34	0.20	−0.8	9.2	9.6	109.98
2.25	77.09 ± 1.00	0.20	−0.8	7.1	7.2	71.50
2.50	54.14 ± 0.81	0.19	−0.7	5.3	5.4	51.20
2.75	41.64 ± 0.68	0.19	−0.6	3.9	4.0	39.97
3.00	34.06 ± 0.59	0.19	−0.5	2.8	3.1	33.02
3.25	29.67 ± 0.52	0.19	−0.4	2.0	2.4	28.97
3.50	27.32 ± 0.49	0.19	−0.3	1.4	1.9	26.81
3.75	25.40 ± 0.45	0.19	−0.2	1.0	1.6	24.99
4.00	23.69 ± 0.43	0.19	−0.1	0.7	1.5	23.35
4.25	23.50 ± 0.41	0.19	0.0	0.5	1.3	23.19
4.50	22.50 ± 0.38	0.19	0.1	0.4	1.3	22.21
4.75	22.71 ± 0.37	0.19	0.1	0.3	1.2	22.43
5.00	22.25 ± 0.36	0.19	0.2	0.2	1.3	21.97
5.25	21.31 ± 0.34	0.19	0.3	0.2	1.3	21.04
5.50	21.42 ± 0.33	0.19	0.3	0.1	1.3	21.14
5.75	21.59 ± 0.32	0.18	0.4	0.1	1.3	21.31
6.00	21.40 ± 0.31	0.18	0.4	0.1	1.3	21.11
6.25	21.34 ± 0.30	0.18	0.5	0.1	1.4	21.05
6.50	20.97 ± 0.30	0.18	0.6	0.0	1.5	20.66
6.75	20.65 ± 0.29	0.18	0.6	0.0	1.5	20.34
7.00	20.58 ± 0.29	0.18	0.7	0.0	1.6	20.25
7.25	21.03 ± 0.28	0.18	0.7	0.0	1.6	20.70
7.50	20.42 ± 0.28	0.17	0.8	0.0	1.7	20.07
7.75	20.59 ± 0.28	0.17	0.9	0.0	1.7	20.23
8.00	20.68 ± 0.29	0.17	0.9	0.0	1.8	20.32
8.25	20.58 ± 0.30	0.17	1.0	0.0	1.8	20.20
8.50	20.11 ± 0.30	0.17	1.1	0.0	1.9	19.72
8.75	20.17 ± 0.31	0.17	1.1	0.0	2.0	19.77
9.00	20.06 ± 0.33	0.16	1.2	0.0	2.0	19.66
9.25	19.66 ± 0.36	0.16	1.3	0.0	2.1	19.25
9.50	20.20 ± 0.41	0.16	1.3	0.0	2.1	19.78

TABLE VI. Summary of differential cross sections. Beam energy = 414 ± 10 MeV, beam spread = ± 30 MeV (HWHM). The correction due to binning (C_B) is the difference between the total correction and the sum of all other corrections given below.

θ_{lab} (degrees)	Measured $\left(\frac{d\sigma}{d\Omega}\right)_m \pm \delta_m$ (mb/sr)	C_{inel} (mb/sr)	Corrections to $(d\sigma/d\Omega)_m$ $\frac{H(\theta)}{(d\sigma/d\Omega)_m}$ (%)	$\frac{G(\theta)}{(d\sigma/d\Omega)_m}$ (%)	$\frac{C}{(d\sigma/d\Omega)_m}$ (%)	Corrected $\frac{d\sigma}{d\Omega}$ (mb/sr)
2.125	88.08 ± 2.13	0.47	−0.8	6.3	6.9	82.03
2.375	56.19 ± 1.67	0.47	−0.8	5.0	5.7	52.97
2.625	42.52 ± 1.37	0.46	−0.6	3.6	4.5	40.61
2.875	34.99 ± 1.20	0.46	−0.6	2.5	3.6	33.72
3.125	28.00 ± 1.10	0.46	−0.5	1.9	3.3	27.08
3.375	26.32 ± 0.99	0.46	−0.3	1.3	2.8	25.59
3.625	24.70 ± 0.94	0.45	−0.2	0.9	2.6	24.06
3.875	25.06 ± 0.90	0.45	−0.2	0.6	2.4	24.46
4.125	21.79 ± 0.83	0.45	−0.1	0.5	2.6	21.23
4.375	21.61 ± 0.82	0.45	0	0.4	2.5	21.09
4.625	22.29 ± 0.79	0.45	0.1	0.2	2.4	21.77
4.875	22.82 ± 0.78	0.44	0.2	0.2	2.4	22.29
5.125	22.58 ± 0.80	0.44	0.2	0.1	2.4	22.06
5.375	20.82 ± 0.80	0.44	0.3	0.1	2.5	20.30
5.625	22.69 ± 0.81	0.44	0.4	0.1	2.4	22.19
5.875	20.89 ± 0.82	0.43	0.4	0.1	2.5	20.38
6.125	20.83 ± 0.83	0.43	0.5	0.0	2.6	20.30
6.375	20.30 ± 0.91	0.43	0.5	0.0	2.7	19.76
6.625	20.70 ± 0.94	0.43	0.6	0.0	2.8	20.13
6.875	19.70 ± 1.03	0.43	0.5	0.0	3.0	19.11
7.125	20.34 ± 1.11	0.42	0.8	0.0	2.9	19.76
7.375	19.83 ± 1.13	0.42	0.8	0.0	3.0	19.25

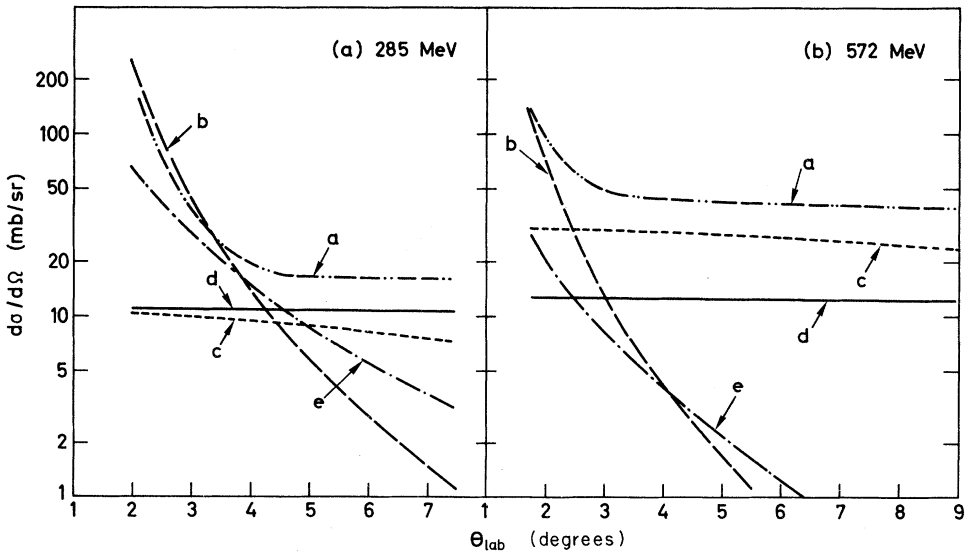

FIG. 8. Proton-proton elastic differential cross sections as a function of the lab scattering angle at (a) 285 MeV and (b) 572 MeV. The curve a is the result of the fit with the phase-shift method with the parameter values noted in Table XI. The contributions due to the Coulomb scattering (curve b), the nuclear non-spin-flip (curve c), the spin-flip scattering (curve d), and the destructive Coulomb-nuclear interference (curve e) are shown separately.

$$C_R(\theta) = R * \left(\frac{d\sigma}{d\Omega} + C_{\text{inel}} + C_M\right) - \left(\frac{d\sigma}{d\Omega} + C_{\text{inel}} + C_M\right). \quad (38)$$

1. Determination of the resolution function $R(\theta)$

Calculation of the resolution function $R(\theta)$ is based on a method developed by Øveras.[19] For a single telescope, the resolution is a convolution of three effects. The first is the multiple scattering in the MWPC, the second is the multiple scattering in the matter between the chambers, and the third is the effect due to the MWPC spatial resolution. The latter has been treated as a Gaussian rather than a constant function over the wire spacing. This has little effect on the final results since six MWPC are used in the reconstruction. For a system with two telescopes, the over-all system resolution function $R(\theta)$ is given by convolution of the distributions for the individual telescopes with the Molière multiple scattering distribution of the matter in between. The target material (LH_2) is not included. With these approximations, $R(\theta)$ is also a Molière distribution with new parameters θ_R and B_R. In order to check the procedure, $R(\theta)$ was convoluted with a Molière distribution for the liquid hydrogen in the target. The resulting function was compared to the angular distribution observed for particles passing straight through the apparatus. Figure 7 shows that the agreement is excellent. Simulated events generated in the Monte Carlo program also show good agreement.

TABLE VII. Summary of differential cross sections. Beam energy = 455 ± 2 MeV, beam spread = ±5 MeV (HWHM). The correction due to binning (C_B) is the difference between the total correction and the sum of all other corrections given below.

θ_{lab} (degrees)	Measured $\left(\frac{d\sigma}{d\Omega}\right)_m \pm \delta_m$ (mb/sr)	C_{inel} (mb/sr)	Corrections to $(d\sigma/d\Omega)_m$ $\frac{H(\theta)}{(d\sigma/d\Omega)_m}$ (%)	$\frac{G(\theta)}{(d\sigma/d\Omega)_m}$ (%)	$\frac{C}{(d\sigma/d\Omega)_m}$ (%)	Corrected $\frac{d\sigma}{d\Omega}$ (mb/sr)
1.75	170.88 ± 1.37	0.66	−0.8	9.8	10.8	152.50
2.00	99.42 ± 1.00	0.66	−0.8	7.4	8.2	91.23
2.25	68.70 ± 0.78	0.66	−0.7	5.2	6.1	64.50
2.50	49.75 ± 0.65	0.65	−0.6	3.8	4.9	47.30
2.75	41.36 ± 0.56	0.65	−0.5	2.6	3.9	39.74
3.00	35.29 ± 0.50	0.64	−0.4	1.8	3.4	34.09
3.25	31.71 ± 0.46	0.64	−0.3	1.2	3.1	30.73
3.50	30.20 ± 0.42	0.63	−0.1	0.8	2.8	29.35
3.75	28.84 ± 0.40	0.63	−0.1	0.6	2.7	28.06
4.00	28.49 ± 0.38	0.63	0.0	0.4	2.6	27.74
4.25	27.51 ± 0.36	0.62	0.1	0.3	2.6	26.79
4.50	27.01 ± 0.34	0.62	0.1	0.2	2.7	26.29
4.75	26.65 ± 0.33	0.62	0.2	0.1	2.7	25.94
5.00	26.20 ± 0.32	0.61	0.3	0.1	2.7	25.49
5.25	26.12 ± 0.30	0.61	0.3	0.1	2.8	25.41
5.50	25.82 ± 0.30	0.60	0.4	0.1	2.8	25.11
5.75	25.71 ± 0.29	0.60	0.4	0.0	2.8	24.99
6.00	25.51 ± 0.28	0.59	0.5	0.0	2.8	24.79
6.25	24.78 ± 0.27	0.59	0.5	0.0	2.9	24.05
6.50	25.29 ± 0.27	0.59	0.6	0.0	2.9	24.55
6.75	24.99 ± 0.26	0.58	0.7	0.0	3.0	24.24
7.00	24.55 ± 0.25	0.58	0.7	0.0	3.1	23.80
7.25	24.55 ± 0.25	0.57	0.8	0.0	3.1	23.79
7.50	24.09 ± 0.25	0.57	0.8	0.0	3.2	23.32
7.75	24.26 ± 0.25	0.57	0.9	0.0	3.2	23.47
8.00	24.23 ± 0.25	0.56	0.9	0.0	3.3	23.43
8.25	23.71 ± 0.25	0.55	1.0	0.0	3.4	22.91
8.50	24.14 ± 0.26	0.55	1.1	0.0	3.3	23.33
8.75	23.97 ± 0.27	0.55	1.1	0.0	3.4	23.16
9.00	23.26 ± 0.29	0.54	1.2	0.0	3.6	22.43
9.25	23.71 ± 0.31	0.54	1.3	0.0	3.5	22.87
9.50	22.96 ± 0.34	0.54	1.4	0.0	3.7	22.11

2. Effect of vertex cuts on the resolution function

The Molière angular resolution function has been written as a Gaussian small-angle part $R_S(\theta)$ plus a large-angle tail $R_L(\theta)$,

$$R(\theta) \approx R_S(\theta) + R_L(\theta) . \tag{39}$$

$R_L(\theta)$ is given by the Rutherford distribution convoluted with the Gaussian part of the resolution. The observed angular distribution P_{obs} is a convolution of $R(\theta)$ with the scattering distribution of the protons in the LH_2 target, P_H,

$$P_{obs} = R * P_H \approx R_S * P_H + R_L * g_H + R_L * (P_H - g_H), \tag{40}$$

where the function g_H is the Gaussian part of the hydrogen scattering distribution and corresponds to the multiple Coulomb scattering. The last term of Eq. (40) corresponds to events with a large scattering angle in the telescopes as well as in the LH_2 target. The probability for these events to pass the vertex minimum distance and track quality cuts is small, and the term can be neglected. The second term corresponds to a large-angle scattering in the telescopes coupled with a small deflection in the LH_2 target. If the scattering is in one of the MWPC, the reconstructed vertex will be far from the LH_2 appendix and the cut on Z_v will eliminate these events. Scattering in the windows of the target is compensated for by the dummy subtraction. Thus the second term can also be neglected. Only the first term with the small-angle part of the resolution function is left, which means that $R(\theta)$ is very well approximated by a Gaussian given by

TABLE VIII. Summary of differential cross sections. Beam energy = 497 ± 2 MeV, beam spread = ±10 MeV (HWHM). The correction due to binning (C_B) is the difference between the total correction and the sum of all other corrections given below.

θ_{lab} (degrees)	Measured $\left(\frac{d\sigma}{d\Omega}\right)_m \pm \delta_m$ (mb/sr)	C_{inel} (mb/sr)	Corrections to $(d\sigma/d\Omega)_m$ $\frac{H(\theta)}{(d\sigma/d\Omega)_m}$ (%)	$\frac{G(\theta)}{(d\sigma/d\Omega)_m}$ (%)	$\frac{C}{(d\sigma/d\Omega)_m}$ (%)	Corrected $\frac{d\sigma}{d\Omega}$ (mb/sr)
1.75	159.76± 1.45	1.20	−0.5	8.1	9.5	144.64
2.00	97.85± 1.07	1.19	−0.5	5.8	7.3	90.69
2.25	69.14± 0.86	1.19	−0.4	4.0	5.8	65.12
2.50	53.26± 0.72	1.19	−0.4	2.8	5.0	50.62
2.75	44.70± 0.63	1.19	−0.3	1.8	4.5	42.71
3.00	40.15± 0.57	1.18	−0.2	1.2	4.1	38.49
3.25	37.41± 0.53	1.18	−0.1	0.8	4.0	35.93
3.50	36.22± 0.49	1.18	0.0	0.5	3.8	34.84
3.75	34.26± 0.46	1.18	0.0	0.4	3.9	32.93
4.00	33.38± 0.44	1.17	0.1	0.3	3.9	32.08
4.25	33.18± 0.42	1.17	0.2	0.2	3.9	31.90
4.50	32.48± 0.40	1.17	0.2	0.1	3.9	31.20
4.75	32.05± 0.39	1.16	0.3	0.1	4.0	30.77
5.00	31.51± 0.37	1.16	0.3	0.1	4.1	30.23
5.25	31.35± 0.36	1.16	0.3	0.1	4.1	30.06
5.50	31.09± 0.34	1.15	0.4	0.0	4.2	29.80
5.75	31.00± 0.33	1.15	0.5	0.0	4.2	29.70
6.00	30.52± 0.32	1.15	0.5	0.0	4.3	29.21
6.25	30.63± 0.32	1.14	0.6	0.0	4.3	29.31
6.50	30.22± 0.30	1.14	0.6	0.0	4.4	28.89
6.75	30.45± 0.30	1.14	0.7	0.0	4.4	29.11
7.00	29.70± 0.29	1.13	0.7	0.0	4.6	28.35
7.25	29.70± 0.29	1.13	0.8	0.0	4.6	28.33
7.50	29.65± 0.29	1.13	0.8	0.0	4.7	28.27
7.75	29.83± 0.29	1.12	0.9	0.0	4.7	28.44
8.00	29.28± 0.29	1.12	1.0	0.0	4.8	27.88
8.25	29.42± 0.30	1.12	1.0	0.0	4.8	27.99
8.50	29.10± 0.30	1.12	1.1	0.0	4.9	27.66
8.75	29.57± 0.32	1.11	1.1	0.0	4.9	28.12
9.00	29.76± 0.34	1.11	1.2	0.0	4.9	28.30
9.25	29.41± 0.36	1.11	1.3	0.0	5.1	27.92
9.50	29.58± 0.40	1.10	1.3	0.0	5.1	28.08

$$R(\theta)\approx R_S(\theta)=(2/\theta_R{}^2)e^{-(\theta/\theta_R)^2} \tag{39'}$$

D. Corrections due to binning

The contents of a bin represent the mean value of the distribution in the interval considered. This is generally different from the value of the distribution at the middle of the bin. For the bin size of 0.25° used, Fig. 6 shows that the fractional correction for this effect is small (<0.02) even in the Coulomb region, and is nearly independent of energy.

E. Stability of the corrections

It was noted earlier that the corrections to the data are dependent on the parameters $\vec{\pi}$ used to describe the cross sections. To study this dependence it is more efficient to treat the corrections for multiple scattering and angular resolution together.

$$C_M(\theta)+C_R(\theta)=\left[\frac{1}{N_{at}}R*M_H-\left(\frac{d\sigma}{d\Omega}\right)^C\right]+R*M_H*\left[\frac{d\sigma}{d\Omega}-\left(\frac{d\sigma}{d\Omega}\right)^C+C_{inel}\right]-\left[\frac{d\sigma}{d\Omega}-\left(\frac{d\sigma}{d\Omega}\right)^C+C_{inel}\right]. \tag{41}$$

TABLE IX. Summary of differential cross sections. Beam energy = 530 ± 2 MeV, beam spread = ±10 MeV (HWHM). The correction due to binning (C_B) is the difference between the total correction and the sum of all other corrections given below.

θ_{lab} (degrees)	Measured $\left(\frac{d\sigma}{d\Omega}\right)_m \pm \delta_m$ (mb/sr)	C_{inel} (mb/sr)	Corrections to $(d\sigma/d\Omega)_m$ $\frac{H(\theta)}{(d\sigma/d\Omega)_m}$ (%)	$\frac{G(\theta)}{(d\sigma/d\Omega)_m}$ (%)	$\frac{C}{(d\sigma/d\Omega)_m}$ (%)	Corrected $\frac{d\sigma}{d\Omega}$ (mb/sr)
1.75	154.57± 2.01	1.74	−0.4	6.9	8.7	141.17
2.00	100.18± 1.53	1.74	−0.4	4.7	6.7	93.43
2.25	73.94± 1.23	1.73	−0.3	3.1	5.6	69.82
2.50	57.68± 1.05	1.73	−0.2	2.1	5.1	54.71
2.75	52.08± 0.94	1.72	−0.1	1.3	4.6	49.67
3.00	46.98± 0.85	1.72	−0.1	0.9	4.5	44.84
3.25	44.22± 0.79	1.72	0.0	0.6	4.5	42.23
3.50	42.70± 0.74	1.71	0.0	0.4	4.5	40.79
3.75	41.83± 0.70	1.71	0.1	0.3	4.5	39.96
4.00	41.34± 0.67	1.70	0.1	0.2	4.4	39.50
4.25	41.30± 0.64	1.70	0.2	0.1	4.4	39.47
4.50	39.36± 0.61	1.70	0.2	0.1	4.6	37.53
4.75	39.44± 0.59	1.69	0.3	0.1	4.6	37.61
5.00	39.05± 0.57	1.69	0.3	0.0	4.7	37.22
5.25	38.27± 0.55	1.69	0.4	0.0	4.8	36.42
5.50	37.90± 0.53	1.68	0.4	0.0	4.9	36.05
5.75	38.48± 0.52	1.68	0.5	0.0	4.8	36.61
6.00	37.23± 0.50	1.68	0.5	0.0	5.0	35.35
6.25	36.76± 0.49	1.67	0.6	0.0	5.1	34.88
6.50	36.50± 0.47	1.67	0.6	0.0	5.2	34.60
6.75	35.52± 0.46	1.67	0.7	0.0	5.4	33.60
7.00	36.90± 0.45	1.67	0.7	0.0	5.3	34.97
7.25	35.75± 0.44	1.66	0.8	0.0	5.5	33.80
7.50	36.49± 0.45	1.66	0.8	0.0	5.4	34.52
7.75	35.92± 0.44	1.66	0.9	0.0	5.5	33.93
8.00	35.09± 0.45	1.65	1.0	0.0	5.7	33.09
8.25	35.11± 0.46	1.65	1.0	0.0	5.7	33.09
8.50	35.60± 0.48	1.65	1.1	0.0	5.7	33.57
8.75	35.26± 0.50	1.64	1.2	0.0	5.8	33.21
9.00	35.92± 0.54	1.64	1.2	0.0	5.8	33.85
9.25	35.53± 0.58	1.64	1.3	0.0	5.9	33.44
9.50	35.42± 0.64	1.64	1.3	0.0	6.0	33.31

The first term, $G(\theta)$, is independent of the parameters $\vec{\pi}$, is most important at small angles, and decreases rapidly. The remaining contribution, $H(\theta)$, depends on $\vec{\pi}$. $H(\theta)$ is relatively small, and has a weak angular dependence since it contains only the interference and nuclear parts of the cross section. Since the largest part of the overall correction $[C_{\text{inel}}(\theta)+G(\theta)]$ is independent of the parameters $\vec{\pi}$, the corrections were calculated only twice: once with the reasonable starting estimates of the parameters, and a second time after an initial convergence of the fits to the data. The corrections $G(\theta)$ and $H(\theta)$ are plotted separately in Fig. 6 to show their relative importance. Tables III–X summarize these different corrections at each of the energies studied.

VI. RESULTS

A. Differential cross sections

In Tables III–X, the measured and corrected differential cross sections, as well as the values of the various individual corrections and the overall correction, are given as a function of θ_{lab} at each of the energies studied. The errors are purely statistical and contain no allowance for uncertainties in the corrections.

No attempt was made during the experiment to obtain the absolute normalization of the data, expressed by K in Eq. (30). The estimated normalization obtained from fits using the phase-shift parametrization is model-dependent and is deter-

TABLE X. Summary of differential cross sections. Beam energy = 572 ± 2 MeV, beam spread = ±5 MeV (HWHM). The correction due to binning (C_B) is the difference between the total correction and the sum of all other corrections given below.

θ_{lab} (degrees)	Measured $\left(\frac{d\sigma}{d\Omega}\right)_m \pm \delta_m$ (mb/sr)	C_{inel} (mb/sr)	Corrections to $(d\sigma/d\Omega)_m$ $\frac{H(\theta)}{(d\sigma/d\Omega)_m}$ (%)	$\frac{G(\theta)}{(d\sigma/d\Omega)_m}$ (%)	$\frac{C}{(d\sigma/d\Omega)_m}$ (%)	Corrected $\frac{d\sigma}{d\Omega}$ (mb/sr)
1.75	140.80 ± 1.75	2.61	−0.5	6.1	8.5	128.86
2.00	91.91 ± 1.34	2.61	−0.4	4.1	7.2	85.31
2.25	71.04 ± 1.11	2.61	−0.3	2.6	6.3	66.53
2.50	60.06 ± 0.96	2.60	−0.2	1.6	6.0	56.47
2.75	53.35 ± 0.87	2.60	−0.1	1.0	5.9	50.20
3.00	47.95 ± 0.79	2.59	−0.1	0.7	6.1	45.02
3.25	48.51 ± 0.74	2.59	0.0	0.4	5.8	45.69
3.50	45.93 ± 0.70	2.59	0.1	0.3	6.0	43.17
3.75	46.60 ± 0.66	2.59	0.1	0.2	5.9	43.87
4.00	44.74 ± 0.62	2.58	0.2	0.1	6.1	42.03
4.25	44.58 ± 0.60	2.58	0.2	0.1	6.1	41.87
4.50	43.35 ± 0.57	2.58	0.2	0.1	6.3	40.64
4.75	43.75 ± 0.55	2.57	0.3	0.0	6.2	41.03
5.00	42.30 ± 0.53	2.57	0.3	0.0	6.4	39.57
5.25	42.68 ± 0.51	2.57	0.4	0.0	6.4	39.94
5.50	42.08 ± 0.49	2.56	0.4	0.0	6.5	39.33
5.75	42.24 ± 0.47	2.56	0.5	0.0	6.5	39.47
6.00	41.43 ± 0.45	2.56	0.5	0.0	6.7	38.65
6.25	41.60 ± 0.44	2.55	0.6	0.0	6.7	38.80
6.50	41.79 ± 0.43	2.55	0.6	0.0	6.7	38.98
6.75	41.43 ± 0.41	2.55	0.7	0.0	6.8	38.60
7.00	40.63 ± 0.40	2.54	0.7	0.0	7.0	37.79
7.25	40.28 ± 0.39	2.54	0.8	0.0	7.1	37.42
7.50	40.12 ± 0.39	2.54	0.8	0.0	7.2	37.24
7.75	39.67 ± 0.38	2.53	0.9	0.0	7.3	36.77
8.00	39.53 ± 0.39	2.53	1.0	0.0	7.4	36.61
8.25	39.39 ± 0.40	2.53	1.0	0.0	7.5	36.46
8.50	39.52 ± 0.41	2.53	1.1	0.0	7.5	36.56
8.75	39.19 ± 0.43	2.52	1.2	0.0	7.6	36.22
9.00	39.17 ± 0.47	2.52	1.2	0.0	7.7	36.17
9.25	39.90 ± 0.52	2.52	1.3	0.0	7.6	36.88
9.50	39.59 ± 0.58	2.51	1.3	0.0	7.7	36.55

mined mainly by the Coulomb part of the distribution. Therefore at all energies, the over-all normalization can be changed without prejudice.

B. Determination of α_p

Fits to the data were made using the two formalisms described in Sec. II.

1. Phase-shift parametrization

Table I gives the values of the six parameters as calculated from the MacGregor phase shifts.[15] The total cross sections were taken from a Saclay compilation.[17] Our measurements are not extensive enough to allow determination of all six parameters, especially for the type II data where the angular range is smaller ($\theta_{max} = 7.325°$ instead of 9.5°) and the statistical errors are 2–3 times bigger. The parameter α' was kept fixed. We noticed, however, that if it were set equal to zero, the fits to the data had a lower probability. The most informative fits are summarized in Table XI. The parameters without errors were fixed in the fitting procedure. The errors correspond to a variation of 1 in the χ^2 of the fit. Figure 8 displays separately at 285 and 572 MeV each of the four contributions to the differential cross section; the pure Coulomb scattering, the non-spin-flip nuclear term, the interference effect, and the spin-flip nuclear cross section, given in Eq. (11) and (17)–(19), respectively. The decrease in the size of the destructive interference term between 285 and 572 MeV is quite noticeable.

2. Classical parametrization

This parametrization has been used by most authors in the analysis of similar experiments.[1,2,4] It is assumed that the non-spin-flip and spin-flip nuclear cross sections are proportional and α_p is usually considered as being independent of t (i.e., $\alpha' = 0$). The summary of various fits using this

TABLE XI. Results of fits to the p-p differential cross sections using the phase-shift parametrization. The values without errors were fixed parameters in the fit. The lines indicated with an asterisk in the $P(\chi^2)$ column are the fits used to normalize the data in Tables III to X.

Energy (MeV)	B Slope parameter [(GeV/c)$^{-2}$]	α_0	a_0 [mb (GeV/c)$^{-2}$]	Probability $P(\chi^2)$	Angular range (degrees)
285	14	0.63 ± 0.04	78	<0.1%	2.125° to
	14	0.90 ± 0.05	56.0 ± 2.0	27% *	7.375°
348	10	0.44 ± 0.04	64	<0.1%	2.125° to
	10	0.67 ± 0.05	47.1 ± 2.4	38% *	7.325°
398	8.2	0.33 ± 0.02	52	<0.1%	1.75°
	8.2	0.46 ± 0.02	44.3 ± 0.9	63%	to
	14.3 ± 2.3	0.52 ± 0.03	45.2 ± 1.0	86% *	9.50°
414	7.8	0.36 ± 0.04	48	7%	2.125° to
	7.8	0.52 ± 0.06	35.1 ± 3.9	30% *	7.375
455	7.6	0.32 ± 0.01	40	<0.1%	1.75°
	7.6	0.35 ± 0.02	38.0 ± 1.0	<0.1%	to
	13.3 ± 1.1	0.42 ± 0.02	38.9 ± 1.1	26% *	9.50°
497	7.4	0.34 ± 0.07	31	1%	1.75°
	7.4	0.29 ± 0.02	36.0 ± 1.4	10%	to
	6.8 ± 0.8	0.28 ± 0.03	35.8 ± 1.4	10% *	9.50°
530	7.3	0.33 ± 0.10	26	<0.1%	1.75°
	7.3	0.19 ± 0.03	39.9 ± 2.6	1%	to
	8.4 ± 0.9	0.21 ± 0.04	40.3 ± 2.7	1.5% *	9.50°
572	7.2	0.27 ± 0.01	22	0.4%	1.75°
	7.2	0.21 ± 0.03	30.2 ± 3.0	2%	to
	6.1 ± 0.5	0.20 ± 0.03	28.8 ± 3.0	4% *	9.50°

parametrization is shown in Table XII. The three parameters α_p, b, and ρ^2 all decrease as the incident kinetic energy increases. In the t region covered, α_p is strongly correlated with the slope b, and ρ^2 is correlated with σ_{tot}. Therefore it is important to quote the value used for σ_{tot} in the fit. The decreasing value of ρ^2 with increasing energy shows that spin dependence decreases as a function of energy. To compare with other authors,[1,2,4] we have also tried fitting our data with $b = 0$ $(\mathrm{GeV}/c)^{-2}$. The probability of the fits is poorer; therefore, comparison of α_p with other results is difficult.

3. *Phase-shift analysis*

Our new data have been included in an existing phase-shift analysis.[20] Figure 9 shows the resulting dependence of α_p versus energy, with its error corridor. The curves labelled a, b, c are results of different calculations by MacGregor,[15] Söding,[3] and Dumbrais.[21]

VII. CONCLUSIONS

Accurate measurements of the p-p elastic differential cross sections have been presented in the energy range between 285 and 572 MeV. Fits to the data were used to determine the ratio $\alpha_0 = \mathrm{Re}\,\varphi_+^N(0)/\mathrm{Im}\varphi_+^N(0)$. The following observations can be made. The value of α_0 is positive and decreases with energy. It varies from 0.9 at 285 MeV to 0.2 at 572 MeV. The values obtained depend on the parametrization used, and a precise formalism is not available at present. The most reliable values of α_p are obtained by including these differential cross sections in a phase-shift analysis. The imaginary part of the non-spin-flip nuclear amplitude, φ_{nf}^N, has a strong exponential t dependence. Its slope parameter B is large, decreases with increasing energy, and approaches from above the slope parameter obtained at higher energy by fitting the whole differential cross section. This indicates a rapidly decreasing contribution from the spin-dependent term, which, however, is still important at 572 MeV. At small an-

TABLE XII. Results of fits using the classical parametrization. Variables without error bars were fixed in the adjustment.

Energy (MeV)	b $[(\mathrm{GeV}/c)^{-2}]$	α_p $(\equiv \alpha_0)$	ρ^2	σ_{tot} (mb)	Probability $P(\chi^2)$	Angular range (degrees)
285	0.3	0.76 ± 0.04	1.94 ± 0.07	24.0	17%	2.125° to
	15.6 ± 9.4	0.90 ± 0.10	2.09 ± 0.12	24.0	20%	7.375°
348	0.4	0.54 ± 0.04	1.60 ± 0.08	24.6	28%	2.125° to
	9.8 ± 7.0	0.65 ± 0.10	1.65 ± 0.09	24.6	30%	7.375°
398	0.5	0.30 ± 0.02	1.41 ± 0.03	25.6	<0.1%	1.75° to
	8.1 ± 1.0	0.48 ± 0.03	1.44 ± 0.03	25.6	77%	9.50°
414	0.55	0.36 ± 0.05	1.09 ± 0.11	27.0	8%	2.125° to
	24.0 ± 6.0	0.70 ± 0.09	0.99 ± 0.11	27.0	64%	7.375°
455	0.6	0.16 ± 0.02	1.06 ± 0.03	28.5	<0.1%	1.75° to
	7.8 ± 0.6	0.38 ± 0.02	1.00 ± 0.03	28.5	3%	9.50°
497	0.7	0.12 ± 0.02	0.87 ± 0.03	30.5	<0.1%	1.75° to
	4.0 ± 0.6	0.24 ± 0.03	0.82 ± 0.03	30.5	1%	9.50°
530	0.9	0.11 ± 0.03	0.91 ± 0.05	32.6	<0.1%	1.75° to
	4.3 ± 0.7	0.17 ± 0.04	0.80 ± 0.05	32.6	0.3%	9.50°
572	1.5	0.33 ± 0.02	0.62 ± 0.05	36.0	<0.1%	1.75° to
	4.2 ± 0.5	0.17 ± 0.03	0.48 ± 0.05	36.0	1%	9.50°

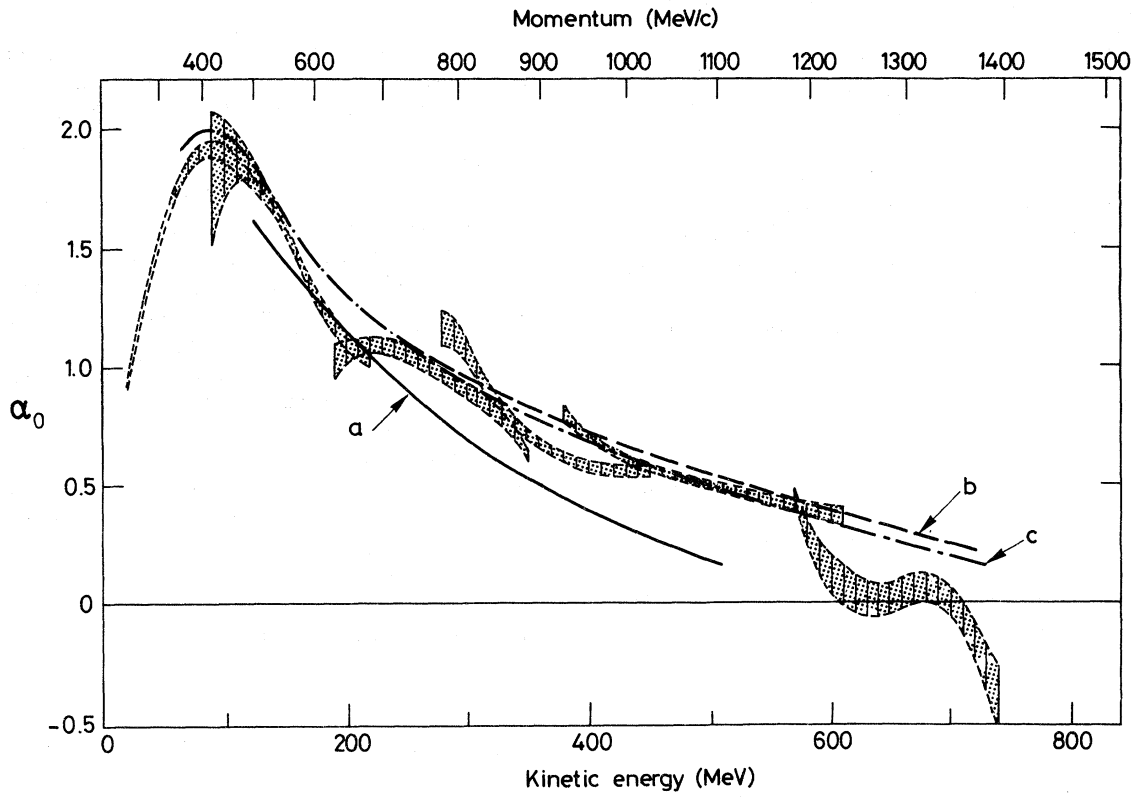

FIG. 9. The ratio α_0 of the real and imaginary parts of the forward p-p non-spin-flip scattering amplitude as a function of energy. The shaded bands are the new phase-shift predictions of Bystricky and Lehar (see Ref. 20), which incorporate the present cross-section data. Curve a represents the MacGregor phase shifts (see Ref. 15), and curves b and c are dispersion relation calculations of Söding (see Ref. 3) and Dumbrais (see Ref. 21), respectively.

gles, it is nearly constant and can be approximated by a second-order polynomial in t. It does not seem to have an exponential t dependence as is assumed at higher energy.

ACKNOWLEDGMENTS

The assistance of Dr. E. G. Michaelis and the CERN SC staff is greatly appreciated. We would like to thank Professor E. Heer for his constant encouragement and for many useful discussions. We also thank Dr. J. Bystricky and Dr. F. Lehar for many useful discussions and exchange of information. This work could not have been done without the aid of the technical staff of the Département de Physique Nucléare et Corpulsculare of the University of Geneva, especially B. Mauron, J. P. Vittet, and E. Perrin. We also thank Professor G. B. Miller, R. Bovet, and P. Lenoir who helped us during the data taking. This work was supported by the Swiss National Funds, the Convention Internationale d'Enseignement du 3ème Cycle de la Physique en Suisse Romande, and the Swiss Institute for Nuclear Research.

---

*Swiss Federal Institute of Technology, Zürich, Switzerland.
†ISN Grenoble; present address: I N2 P3 Paris, France.

[1]L. M. C. Dutton, R. J. W. Howells, J. D. Jafar, H. B. Van der Raay, Phys. Lett. 25B, 245 (1967).
[2]L. M. C. Dutton and H. B. Van der Raay, Phys. Lett. 26B, 679 (1968).
[3]P. Söding, Phys. Lett. 8, 285 (1964).
[4]A. A. Vorobyov, A. S. Denisov, Yu. K. Zalite, G. A. Korolev, V. A. Korolev, G. G. Kovshevny, Ye. M. Maev, V. I. Medvedev, G. L. Sokolov, G. Ye. Solyakin, E. M. Spiridenkov, I. I. Tkach, and V. A. Schegelsky, Phys. Lett. 41B, 639 (1972).
[5]D. Aebischer, Ph.D. thesis, University of Geneva, Switzerland, 1975 (unpublished).
[6]D. Aebischer, R. Bovet, B. Favier, G. Greeniaus,

R. Hess, A. Junod, C. Lechanoine, J. C. Niklès, D. Rapin, J. P. Vittet, and D. Werren, Nucl. Instrum. Methods 117, 131 (1974).
[7]D. Aebischer, B. Favier, G. Greeniaus, R. Hess, A. Junod, C. Lechanoine, J. C. Niklès, D. Rapin, and D. Werren, report presented at the Fourth International Symposium on Polarization Phenomena in Nuclear Reactions, Zürich, 1975 (unpublished); A. Junod, Ph.D. thesis, ETH Zürich (unpublished).
[8]J. C. Niklès, Ph.D. thesis, University of Geneva, Switzerland (unpublished). D. Aebischer, B. Favier, G. Greeniaus, R. Hess, A. Junod, C. Lechanoine, J. C. Niklès, D. Rapin, and D. Werren, Nucl. Phys. (to be published).
[9]D. Aebischer, B. Favier, G. Greeniaus, R. Hess, A. Junod, C. Lechanoine, J. C. Niklès, D. Rapin, and D. Werren, Nucl. Instrum. Methods 124, 49 (1975).
[10]M. L. Goldberger, M. T. Grisaru, S. W. MacDowell, and D. Y. Wong, Phys. Rev. 120, 2250 (1960).
[11]E. Leader and R. C. Slansky, Phys. Rev. 148, 1491 (1966).
[12]H. A. Bethe, Ann. Phys. (N.Y.) 3, 190 (1958).
[13]M. P. Locher, Nucl. Phys. B2, 525 (1967).
[14]N. H. Buttimore, Westfield College, London report, 1967 (unpublished).
[15]M. H. MacGregor, R. A. Arndt, and R. M. Wright, Phys. Rev. 182, 1714 (1969).
[16]D. Aebischer, E. Heer, R. Hess, B. Mauron, and D. Werren, Nucl. Instrum. Methods 99, 405 (1972).
[17]J. Bystricky, F. Lehar, and Z. Janout, Saclay Report No. CEA-N-1547, 1972 (unpublished).
[18]G. Z. Molière, Z. Naturforsch. 3(a) 78 (1948); H. A. Bethe, Phys. Rev. 89, 1256 (1953).
[19]H. Øveras, CERN Yellow Report No. 63-9; CERN internal report NP-DH6 73-3 (unpublished).
[20]J. Bystricky and F. Lehar, report presented at the Fourth International Symposium on Polarization Phenomena in Nuclear Reactions, Zürich, 1975 (unpublished).
[21]O. V. Dumbrais, Yad. Fiz. 13, 1096 (1971) [Sov. J. Nucl. Phys. 13, 626 (1971)].